Critical thickness for high-remanent single-domain configurations in square ferromagnetic thin platelets

D. Goll, G. Schütz, and H. Kronmüller

Max-Planck-Institut für Metallforschung, Heisenbergstraße 1, D-70569 Stuttgart, Germany

By means of three-dimensional micromagnetic finite element modeling, zero-field magnetization patterns of ferromagnetic thin film elements of square shape are simulated and energetically compared. The geometry of the sample (edge length a, thickness D) and its intrinsic material parameters (hardness Q) are systematically varied. Based on the results the corresponding phase diagram is set up which identifies a quasihomogeneous single-domain phase (C, S, and flower states) and a vortex phase (Landau state). For the transition between the two phases a material- and edge-length-dependent critical film thickness is found. The numerical results can be confirmed qualitatively using a simple analytical model calculation.

I. INTRODUCTION

An important prerequisite for all kinds of magnetic recording media are homogeneously magnetized small particles or thin platelets of ferromagnetic and ferrimagnetic materials with uniaxial anisotropy, in which two stable directions of the magnetization may occur. Between these two ground states the particle/platelet can be switched reproducibly by applying an external magnetic field. Depending on its positive or negative magnetization orientation each element can store information as one single bit ("0" or "1") defining the binary number system. Whereas the conventional data storage and the magneto-optical recording are based on in-plane or vertical orientations of the magnetic bit,[1] respectively, single-domain thin film elements are currently in great demand for new integrated magnetoelectronic devices such as nonvolatile magnetic memory and spin-valve magnetic field sensors.[2–4] The magnetization pattern in thin film elements represents a compromise between the minimization of the different competing contributions to the total energy, i.e., stray field energy, magnetocrystalline anisotropy energy, and exchange energy. Besides the geometry of the elements (shape, size, thickness) their magnetic structure also depends on the material, microstructure and magnetic prehistory.

Based on experimental and numerical investigations[5] in soft magnetic thin films of square shape, the different magnetization patterns found at zero magnetic field can be assigned to two main types which are schematically shown in Fig. 1. The high-remanent states (C state, S state, and flower state) are characterized by a high average magnetization with quasiclosure domains formed at the front sides of the platelet. The main feature of the low-remanent state (vortex state) is the vanishing average magnetization resulting from the flux closure domain pattern composed of four domains which are separated from each other by 90° Néel walls. In thin film elements of rectangular shape[6–8] the vortex can be shifted, leading to an asymmetric Landau structure. Further low-remanent domain patterns occurring exclusively in rectangular platelets are the more complex Landau structure with a cross-tie wall and the diamond structure composed of seven domains, where two vortices exist.[6–8] All magnetization arrangements efficiently minimize the magnetic surface poles with a low cost of exchange energy and anisotropy energy by limiting inhomogeneities in the magnetic structure to small regions. In general, the magnetization pattern with the smallest total sum of the energy contributions is the energetically most favorable configuration.

To optimize the quasihomogeneous magnetization patterns for magnetic data storage it is essential to know about the stability criteria responsible for the single-domain behavior. Naturally, a very coarse approximation can be derived from the simple consideration that the critical size of the specimen must be of the order of the domain wall width to avoid domain formation. Furthermore, analytical calculations (which however can only solve a few problems rigorously) have provided useful estimations of the critical size of magnetic particles of spherical[9,10] and prolate spheroidal shapes[11] under which the magnetic domain formation should be completely suppressed, resulting in uniformly magnetized nanomagnets which behave as single giant spins. From an experimental point of view, Elmore[12] discovered the single-domain behavior in small magnetite particles. Furthermore, Cowburn and co-workers[13,14] previously studied the magnetization pattern of submicron disc shaped supermalloy nanomagnets by using a high-sensitivity magneto-optical method, and delineated an experimental phase diagram. This phase diagram derived in diameter and thickness contained a vortex phase and a single-domain phase. For discs of diameters of 100 nm a critical thickness of 15 nm was found.

Recent numerical computations by Rave *et al.*[15] and Hertel and Kronmüller,[16] based on the finite element method (FEM) determined the single-domain limit of ferromagnetic cubes. This problem was treated by the μMAG micromagnetic standard problem (No. 3) (Ref. 17) for achieving reliable tests of numerical algorithms. The finite element method
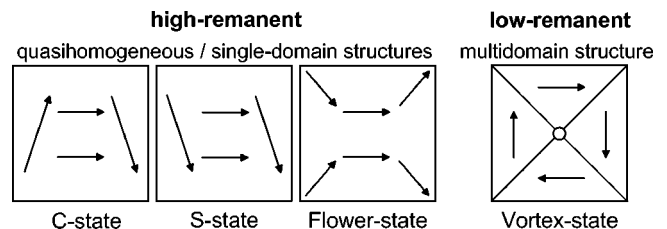

FIG. 1. Schematic representation of possible domain configurations in a square soft magnetic thin platelet.

has been proven to be a rather effective and flexible method from first principles in the framework of micromagnetism.[18–27] It allows the calculation of magnetic ground states including their spin configurations, as well as the magnetization processes and corresponding hysteresis loops of small particles, complex particle systems and thin platelets. Examples of such investigations are papers by Fischer *et al.*[21] where the critical diameters of single domain soft magnetic spheres embedded within a hard matrix have been determined, and by Hertel *et al.*[23] where the existence of sheared Landau structures in thick permalloy films has been found. Magnetization processes and spin configurations in nanocrystalline systems depending on particle sizes and grain sizes are investigated by Schrefl *et al.*,[24] Fischer *et al.*,[25] Novosad *et al.*,[26] and Guslienko *et al.*[27] In the case of rectangular platelets it has been shown in the framework of the standard problems[17] that the energies of C, S, and flower states are very similar. Consequently, the determination of the stray field requires a careful consideration because the critical thickness depends sensitively on the stray field energy. It is the aim of this paper to investigate by means of micromagnetic FEM simulations the influence of the thickness of a square thin platelet on the total energy of the different domain configurations, whereby the edge length of the platelet and its intrinsic material parameters are systematically modified.

II. MICROMAGNETIC FINITE ELEMENT MODELING

To calculate the magnetic structures and energies of the squared platelets the global energy of the sample is directly minimized by means of micromagnetic FEM, which discretizes the specimen by a three-dimensional mesh of irregular tetrahedra. In the following the basics of the algorithm are presented (for details, see Ref. 28).

A. Micromagnetism

The equilibrium configuration of the magnetization usually is obtained from a minimization of the Gibbs free energy composed of exchange energy G_A, magnetocrystalline energy G_K, stray field energy G_S, and magnetostatic energy G_H (the latter, so-called Zeeman, term can be omitted by considering remanent magnetic structures without any external field) with respect to the angular arrangement of the spontaneous polarization $J_S = \mu_0 M_S$ (M_S: is the spontaneous magnetization) under the constraint $|J_S| = J_S = \text{const}$. The total Gibbs free energy for a uniaxial crystal in the remanent state with the easy axis oriented in-plane and parallel to one edge is given by

$$G = G_A + G_K + G_S = \int \left[A \sum_i \left[\nabla \gamma_i(\vartheta, \varphi) \right]^2 \right.$$

$$\left. + K_1 \sin^2 \alpha(\vartheta, \varphi) - \frac{1}{2} H_S \cdot J_S \right] dV, \qquad (1)$$

where A denotes the exchange constant and K_1 the anisotropy constant. γ_i are the direction cosines of J_S. ϑ and φ are the polar and azimuthal angles of J_S in a spherical coordinate

TABLE I. Material parameters, hardness Q, and exchange lengths l_S and l_K of different magnetic materials.

Material	J_S (T)	K_1 (J/m³)	A (pJ/m)	Q	l_S (nm)	l_K (nm)
$Ni_{80}Fe_{20}$	1.0	5.0×10^2	13	0.0013	5.7	161.2
Fe	2.15	4.6×10^4	25	0.025	3.7	23.3
Co	1.8	4.0×10^5	13	0.310	3.2	5.7
$Nd_2Fe_{14}B$	1.61	4.3×10^6	7.7	4.300	2.7	1.3

system, and α describes the angle between the polarization J_S and the easy direction of the layer. The stray field H_S is the magnetic field which results from the magnetic moments of the material. It should be noted that FEM utilizes, only at the nodes, the values $\gamma_i(\theta, \varphi)$ and H_S (by means of U or A; see below) for the minimization, whereas the intermediate values are determined by a linear interpolation. The minimization itself is performed using the conjugate gradient technique.[29]

The range of the different interactions is described by the following two exchange lengths:[30]

$$l_S = \sqrt{\frac{2 \mu_0 A}{J_S^2}}, \quad l_K = \sqrt{\frac{A}{K_1}}. \qquad (2)$$

These critical lengths (in particular the smallest one) govern the extension of regions with strong spin inhomogeneity, as, e.g., domain walls or singularities of vortices, under the influence of the stray field energy (l_S) and crystal anisotropy (l_K), and therefore the magnetic structure itself. The exchange lengths sensitively depend on the magnetic hardness Q ($Q = 2 \mu_0 K_1 / J_S^2$) and consequently on the intrinsic magnetic parameters K_1, J_S and A of the material. According to Table I, the larger the hardness Q the smaller are the exchange lengths. In the case of permalloy the smallest exchange length is $l_S = 5.7$ nm, whereas in the case of $Nd_2Fe_{14}B$ the smallest exchange length is given by $l_K = 1.3$ nm. Obviously, in soft magnetic materials the stray field energy mainly determines the spin-configuration whereas in hard magnetic materials the magnetocrystalline energy becomes dominant.

B. Stray field energy

To handle the nonlocal nature of the long-range stray field term in the case of an irregular discretization mesh, two alternative variational approaches are used for the numerical calculation of upper and lower bounds of the stray field energy—the vector potential method and the scalar potential method. These methods are based on the two Brown's inequalities or functionals,[31,32] which contain only local variables. To achieve the exact value for the stray field energy, the former method minimizes the functional Ψ,

$$G_S \leq \frac{1}{2 \mu_0} \int_\infty (B - J_S)^2 dV = \Psi, \qquad (3)$$

with constraint $\nabla \times \boldsymbol{B} = 0$, i.e., $\boldsymbol{B} = \nabla \times \boldsymbol{A}$ with respect to the vector potential $\boldsymbol{A} = (A_x, A_y, A_z)$. The latter method maximizes the functional Φ,

$$G_S \geq -\frac{\mu_0}{2} \int_\infty \boldsymbol{H}_S^2 \, dV - \int_V \boldsymbol{H}_S \cdot \boldsymbol{J}_S \, dV = \Phi, \tag{4}$$

with constraint $\nabla \times \boldsymbol{H}_S = 0$, i.e., $\boldsymbol{H}_S = -\nabla U$ with respect to the scalar potential U. Hereby, the integrals extend either over the magnets volume V or the total volume (including the nonmagnetic area outside the sample).

To avoid the open boundary problem the bijective or parallelepiped shell transformation[28,33] is applied. This spatial transformation maps the external space into six nonmagnetic finite segments encapsulating the ferromagnetic layer, consequently, changing the open boundary problem into a closed one. In addition, the platelet is embedded in two nonmagnetic layers to improve the edge ratio of the inner space. For the FEM calculations not only the inner space (the magnetic layer) but also the outer space (the two nonmagnetic layers and the six nonmagnetic finite segments) have to be discretized by the three-dimensional mesh of tetrahedra.

A stable solution for the stray field energy is found much faster using the functional Ψ. The reason for this is that in the vector potential method the minimization with increasing numbers of iterations leads to a monotonous approach to the true equilibrium values of ϑ and φ whereas in the case of the scalar potential method the maximization with increasing numbers of iterations leads to a (decreasing) fluctuation of the variables ϑ and φ.[21]

In order to test the precision obtained by using the two functionals Ψ or Φ the stray field energy of a homogeneously magnetized ($G_{ex} = 0$, $G_K = 0$) square of edge length 1 μm and thickness 20 nm has been calculated for different numbers of finite elements in inner and outer space. These numerical results have been compared with the precise analytical result, $G_S = (1/2) N \mu_0 M_S^2$, using Aharoni's calculation[34] for the effective demagnetization factor, N, of parallelepipeds ($p = D/a$; D is the film thickness and a the edge length of the square),

$$N = \frac{1}{2} - \frac{1}{2\pi}\left[\left(p - \frac{1}{p}\right)\ln\left(\frac{\sqrt{p^2+2}+1}{\sqrt{p^2+2}-1}\right) + \frac{2}{p}\ln(\sqrt{2}+1)\right.$$

$$+ p\ln\left(\frac{\sqrt{p^2+1}-1}{\sqrt{p^2+1}+1}\right) + 2\arctan\left(\frac{1}{p\sqrt{p^2+2}}\right)$$

$$+ \frac{2(1-p^2)}{3p}\sqrt{p^2+2} + \frac{2(1-p^3)}{3p} - \frac{2\sqrt{2}}{3p} + \frac{2}{3}\sqrt{p^2+1}$$

$$\left. \times\left(2p - \frac{1}{p}\right)\right], \tag{5}$$

which can be simplified for thin films ($p \leq 0.15$) by means of various Taylor series:

$$N \approx \frac{1}{2\pi}\left[-2p\ln p + \left(-2\ln\frac{\sqrt{2}+1}{2} + 2\sqrt{2} - 1\right)p\right]. \tag{6}$$

According to Fig. 2 the scalar potential method underesti-

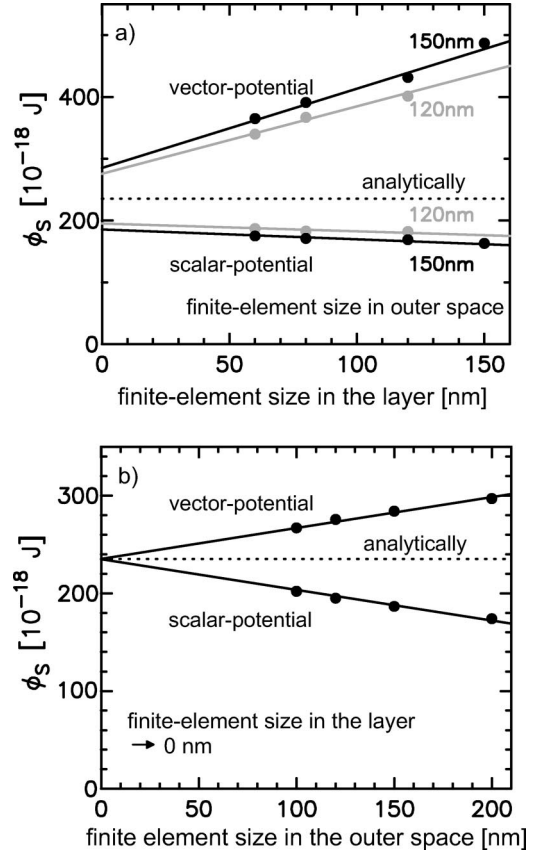
FIG. 2. Test of the precision of the scalar and the vector potential for the case of a homogeneously magnetized quadratic platelet 1 μm$\times$1 μm $\times$20 nm as a function of the size of the finite elements in the layer (a) and outer space (b) and comparison with the precise analytical result. Even when the number of finite elements in the magnetic layer has been optimized, the exact (analytical) value is only obtained after additional optimization of the number of finite elements outside the platelet.

mates throughout the stray field energy, whereas the vector potential method overestimates it. To achieve the correct (analytical) results for the stray field energy a double-extrapolation process has to be performed. In a first step the stray field energy is extrapolated for a given finite element size in the outer space to an infinite number of elements in the magnetic layer. In a second step the stray field energy is extrapolated for the optimized finite element size in the layer (≈ 0 nm) to an infinite number of elements in the outer space. From this second extrapolation step it becomes evident, that for any given finite element size in the outer space and infinite small finite elements in the layer the analytical value for the strayfield energy is just given as the average of the energy values obtained by the vector-potential method and the scalar-potential method. Here it should be noted that such an extrapolation has to be performed for each thickness of the platelet. When the stray field of the magnetic structure has been determined numerically, the affiliated arrangement of the magnetization with minimum energy can be calculated. The alternate determination of the magnetization pattern and its stray field has to be repeated iteratively as long as the process results in a self-consistent solution.
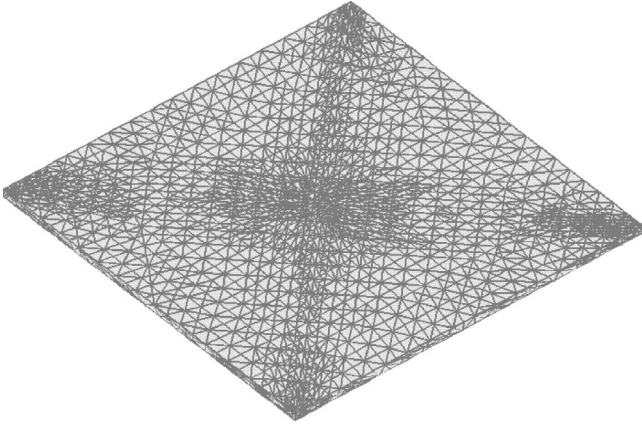
FIG. 3. Finite element mesh of a quadratic permalloy platelet in the vortex state showing the increase of the nodal point density near domain walls and the singular point. As the mesh refinement is performed predominantly in the narrow inhomogeneous regions and not in the widely extended homogeneous regions of the domains, CPU time is dramatically saved.

C. Adaptive mesh refinement

In order to calculate the different energy contributions to the total energy of the magnetization patterns precisely, in the regions of high gradients of the magnetization direction the mesh length should be smaller than the exchange lengths ($\leq l_S$ for soft magnetic materials, and $\leq l_K$ for hard magnetic materials). To resolve the details of the magnetization in regions of strong inhomogeneities the mesh length of the three-dimensional FEM grid is adjusted to the changes of the direction of J_S by the method of the so-called adaptive mesh refinement.[28] This is performed either by bisectioning the tetrahedra by adding new nodal points on the edges of the tetrahedra (*h*-type refinement) or by moving the nodal points toward the regions of higher gradients of the magnetization directions (*r*-type refinement).[35–37] The details of the application of these two methods for the local increase of the discretization density were described in Ref. 28. Especially the *h*-type refinement method is well suited for a description of spin singularities where the magnetization is perpendicular to the surface. On the other hand, the regions of a more or less homogeneous arrangement of the magnetization can be calculated with high accuracy even for a comparatively coarse mesh. As an example, Fig. 3 shows the mesh refinement of a square permalloy thin film element for the vortex state near the 90° domain walls and the singular point. After each construction of a new mesh the magnetization has to be calculated from the minimization of the magnetic Gibbs free energy. This procedure is repeated until the change of the total Gibbs free energy approaches a fixed limit. With adaptive meshing methods reliable calculations of the magnetic structure has become possible whose sizes are considerably larger than the smallest exchange length of the material.

III. THICKNESS DEPENDENCE OF MAGNETIZATION STRUCTURES

The FEM calculations show that four different metastable magnetic structures (C, S, flower, and vortex states) may
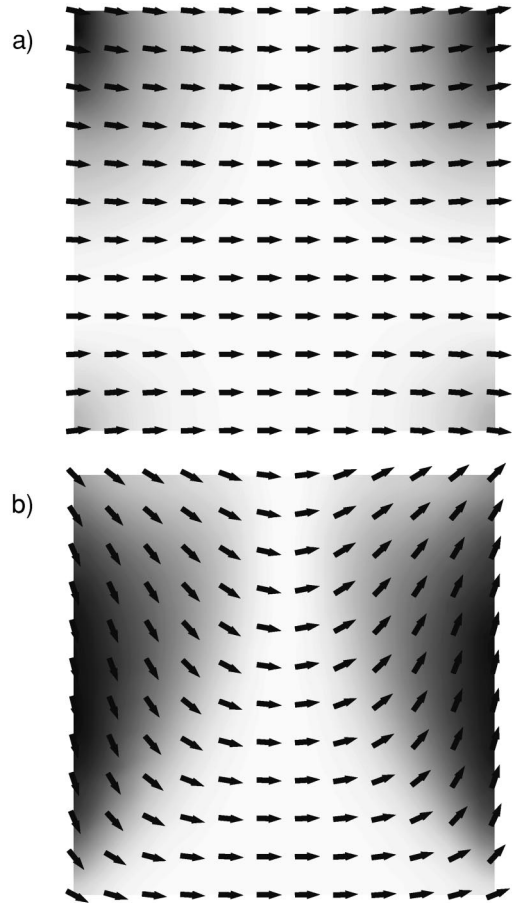

FIG. 4. High-remanent state of C-state configuration obtained by FEM calculations for a square permalloy platelet ($a = 1$ μm) of thicknesses 2 nm (a) and 20 nm (b).

exist in square thin platelets at zero magnetic field. Hereby, the transition between the configurations in order to transform into one with a lower Gibbs free energy often is prevented by large energy barriers. However, in real materials with defects a large number of nucleation centers exist with locally reduced energy barriers which promote the transition into the lowest energy configuration. In the following, it will be shown that the transition depends on the thickness and edge length of the platelet and on its material parameters.

A. Soft magnet material: permalloy

The quasihomogeneous C- and S-state configurations are achieved by suitable modifications of the basic single-domain starting configuration. In fact, the C state forms if the initial state is symmetrical to the symmetry axis whereas the S state develops in the case of a broken symmetry. In Fig. 4 the C state and in Fig. 5 the S state of a square permalloy platelet ($a = 1$ μm) can be seen for two different thicknesses. Both C and S states are developed significantly more distinctly in the case of the thicker layer of $D = 20$ nm in thickness, showing in the magnetization distribution at the front sides of the platelet the quasi-closure end domains of the typical C or S forms within a region of width $l_K = 161$ nm. In contrast, for a layer thickness of 2 nm the

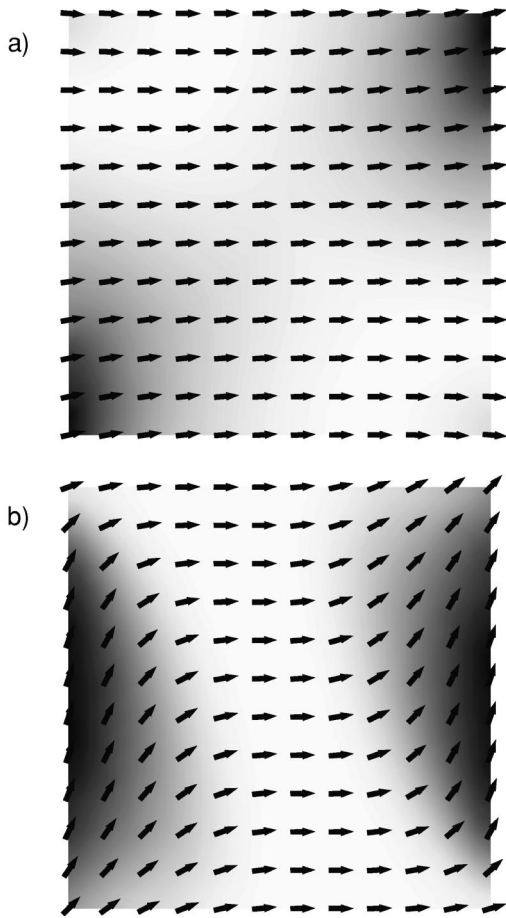FIG. 5. High-remanent state of S-state configuration obtained by FEM calculations for a square permalloy platelet ($a = 1$ μm) of thicknesses 2 nm (a) and 20 nm (b).
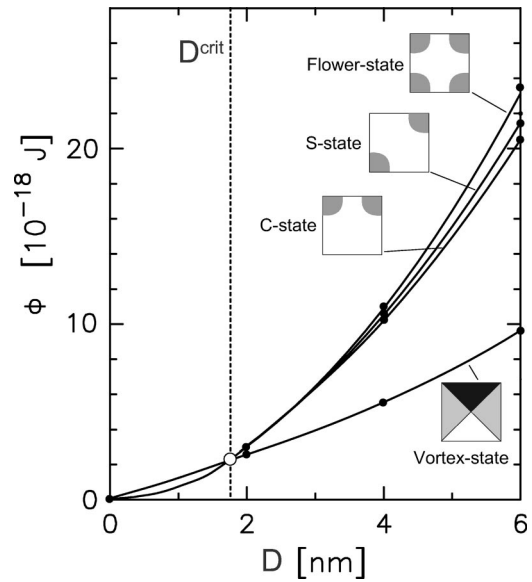

FIG. 6. Total energies Φ obtained by the FEM method for the different types of spin configurations in a square permalloy thin platelet of edge length 1 μm as a function of the layer thickness D. D^{crit} denotes the critical thickness for which a phase transition between the quasihomogeneous state and the vortex state takes place.

magnetization deviates only slightly from the direction of the easy axis, nevertheless still showing a C-like/S-like magnetization pattern with a marginal flower contribution. The flower state which forms directly from the high-field saturated (single-domain) state as a further quasihomogeneous spin configuration is represented in Fig. 8(a) for the permalloy platelet of dimensions 1 μm$\times$1 μm$\times$2 nm. Here the inhomogeneous spin regions occur symmetrically in all four edges of the platelet. With increasing layer thickness, the distinction of the inhomogeneous areas visibly increases as in the case of the C or S state. However, if the thickness of the platelet becomes larger than 6 nm the flower state is found to be unstable.

The low-remanent Landau-type state is obtained if the starting configuration corresponds to a two domain state with two domains magnetized parallel and antiparallel to each other along the easy axis. In the case of permalloy the vortex state is the highest symmetrically, with a well developed vortex in its center in which the magnetization is oriented perpendicular to the layer [see Fig. 7(a)]. This flux-closure configuration is invariant with respect to the layer thickness. In Fig. 6 the different magnetization patterns possibly appearing in the (1×1 μm^2) permalloy platelet are energetically compared with each other as a function of the layer thickness. In

principle, the energies of all configurations increase with increasing thickness. Moreover, for all configurations the stray field energy is the dominating energy contribution, and even in the case of the low-remanent type II configuration, the stray field energy exceeds the increased exchange energy. As a consequence of the high stray field energy resulting from the surface charges, the four domain state for thicker platelets has the lowest total Gibbs free energy. With the decreasing thickness of the platelet, however, the magnetostatic stray field energy decreases more rapidly than the wall energy. Therefore, at a certain critical thickness the total energy of the quasihomogeneous states becomes lower than that of the four domain state, so that the quasihomogeneous states become the energetically most favorable configurations. The numerical calculations show that the transition for permalloy takes place at 1.8 nm. For this layer thickness the three types of quasihomogeneous states are energetically degenerated within the numerical errors of $<10^{-19}$ J. The degeneration is removed for layers thicker than 3 nm, where the C state has the lowest energy minimum of the quasihomogeneous states, followed by the S state. The reason for this could be that in the C-state configuration the distance between the attracting positive and negative surface charges is significantly smaller than in the S-state structure. The flower state, finally, is the energetically most unfavorable quasihomogeneous configuration because its increased exchange energy and inefficiently reduced surface charges are stable only up to a sample thickness of 6 nm.

B. Variation of the magnetic hardness

The critical thickness for which the energetical switching between the quasihomogeneous configurations and the four domain state occurs also depends on the magnetic hardness
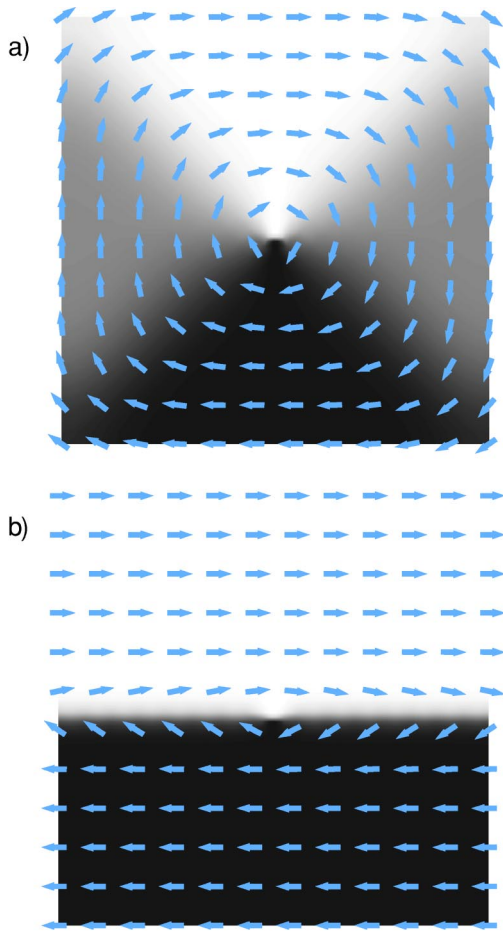
FIG. 7. Low-remanent state of Landau configuration (multido-main state) achieved by FEM calculations for a square thin platelet ($a=1$ μm, $D=2$ nm) of different materials: (a) permalloy and (b) cobalt.

FIG. 8. High-remanent state of flower state configuration re-ceived by FEM calculations for a square thin platelet ($a=1$ μm, $D=2$ nm) of different materials: (a) permalloy and (b) cobalt.

Q of the material. As presented in Fig. 7(a), the high-symmetric vortex state is only developed for very soft uniaxial magnetic materials like permalloy. Actually, with increasing hardness Q, as for Co according to Fig. 7(b), the domain walls are pressed more and more in the direction of the easy axis of the layer whereby the central vortex increas-ingly loses importance. In other words, for sufficiently hard magnetic materials, e.g., for $Nd_2Fe_{14}B$, the four 90° Néel walls have changed to one 180° Néel wall and the vortex has disappeared. It is noteworthy that the transformation ob-served only occurs for uniaxial magnetic materials. In the case of cubic anisotropy the low-remanent vortex-state re-mains high-symmetric up to highest Q values.

A very similar behavior is observed for the flower state, illustrated in Fig. 8 for permalloy and Co. With increasing hardness Q the extensions of the inhomogeneous spin re-gions at the corners are significantly reduced, reflecting the reduction of the exchange length l_K with increasing magne-tocrystalline anisotropy. Here it should be mentioned that for hard magnetic materials, as, e.g., for Co and $Nd_2Fe_{14}B$, the flower state is the only stable quasihomogeneous magnetic structure. In fact, it turns out that the C and S states in hard

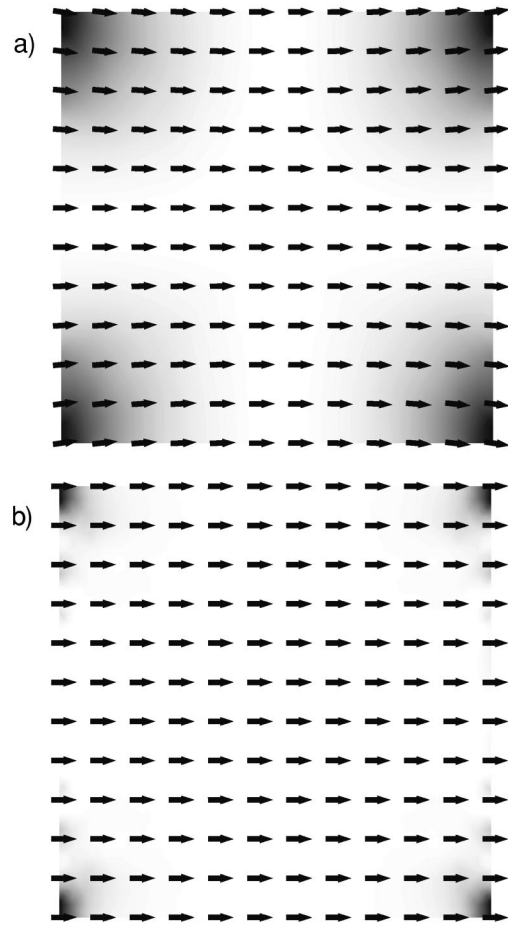magnetic materials are unstable arrangements for the magne-tization. The larger the hardness Q of the material, the larger the critical thickness D^{crit} for which the quasihomogeneous (flower) state becomes energetically unfavored for a given
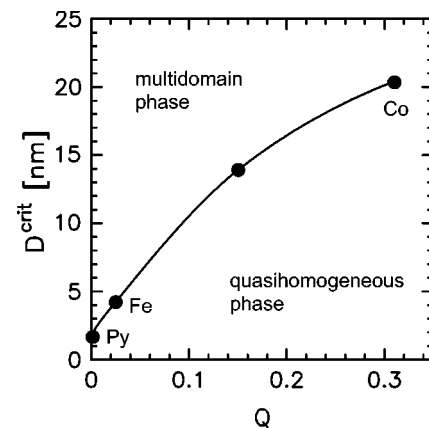

FIG. 9. Numerically determined ($Q-D^{crit}$) phase diagram of the lowest-energy magnetization distribution in square thin platelets of edge length 1 μm. $Q=0.15$ corresponds to a fictitious magnetic material ($K_1=240000$ J/m^3, $A=20$ pJ/m, and $J_s=2.0$ T).
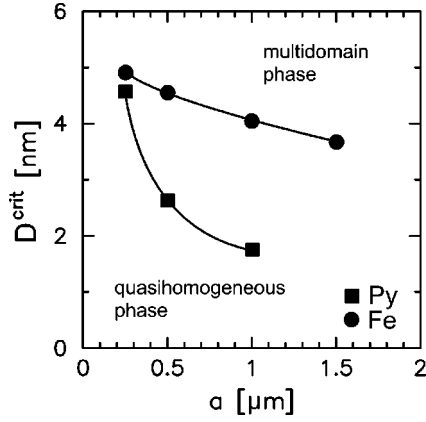
FIG. 10. Numerically determined $(a-D^{\text{crit}})$ phase diagram of the lowest-energy magnetization distribution in square thin platelets of iron and permalloy.

FIG. 11. Determination of the critical thickness of a square permalloy platelet ($a=1$ μm) by means of an analytical model calculation.

geometry of the platelet. This becomes obvious from Fig. 9, where the phase diagram of the lowest-energy magnetization distribution for a square (1×1 μm^2) platelet is shown to depend on the platelet hardness and critical thickness. Below the phase boundary vortex nucleation becomes impossible, and the quasihomogeneous state has the lowest total energy. The phase transition takes place spontaneously as a first order phase transition, whereby for larger Q the flower state becomes dominant and for smaller Q ($\leqslant 0.02$) the C state dominates.

C. Variation of the edge length

An analogous phase diagram can be set up as a fuction of the edge length a of the square platelet (see Fig. 10). Accordingly, for a given material the critical thickness is clearly shifted to larger values when the edge length is appropriately diminished. The magnetization pattern itself is independent of the scaling.

IV. COMPARISON WITH ANALYTICAL MODEL CALCULATIONS

In a first approximation the critical thickness D^{crit} resulting from the numerical calculation can be determined from a simple analytical model calculation, which compares the homogeneous magnetization state (where the total energy arises from the stray field energy only) energetically with the four domain state (where the total energy is determined by the wall energy), whereby the latter state is supposed to be composed of four 90° Néel walls. For thin platelets, the total energy of the homogeneous state obeys the equation

$$\Phi_S=\frac{1}{2\mu_0}J_S^2 N a^2 D,\tag{7}$$

whereby N is given by Eq. (6). On the other hand, the total energy of the four domain state can be obtained from the following formula:
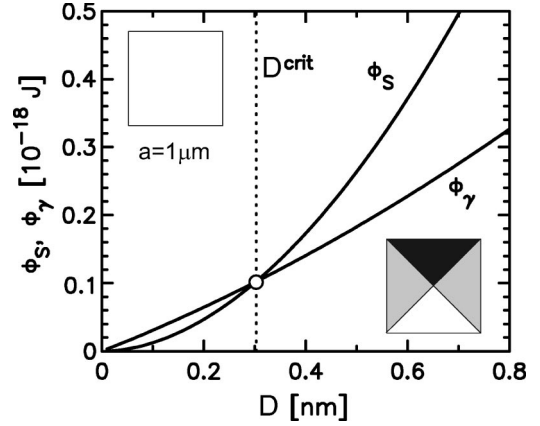
$$\Phi_\gamma=2\sqrt{2}\,\gamma_N^{90}aD.\tag{8}$$

Here γ_N^{90} denotes the wall energy of a 90° Néel wall which can be derived from the bulk relation

$$\gamma_N^{90}=0.32\gamma_N^{180}\tag{9}$$

In turn, for γ_N^{180} of a Néel wall in an infinite film with thickness D according to Aharoni[38] the following equation is valid:

$$\gamma_N^{180}=\frac{2\pi A}{\Delta_N}(\sqrt{2}-1)+\frac{\pi\Delta_N K_1}{2}+\frac{\pi J_S^2\Delta_N}{4\mu_0}\left[1-\frac{2\Delta_N}{D}\right.$$
$$\left.\times\ln\left(1+\frac{D}{2\Delta_N}\right)\right],\tag{10}$$

with the wall width Δ_N which obeys the relation

$$\frac{2A}{\Delta_N^2}(\sqrt{2}-1)=\frac{K_1}{2}+\frac{J_S^2}{2\mu_0}\left[\frac{1}{2}-\frac{2\Delta_N}{D}\ln\left(1+\frac{D}{2\Delta_N}\right)\right.$$
$$\left.+\frac{\Delta_N}{2\Delta_N+D}\right].\tag{11}$$

For thin films ($D<\Delta_N$) Eqs. (10) and (11) can be simplified by making use of different Taylor series resulting in

$$\Delta_N=\sqrt{\frac{4A}{K_1}(\sqrt{2}-1)}\left(1-\frac{1}{64(\sqrt{2}-1)}\frac{J_S^2 D^2}{\mu_0 A}\right),\tag{12}$$

$$\gamma_N^{180}=2\pi\sqrt{\sqrt{2}-1}\sqrt{AK_1}+\frac{\pi J_S^2}{16\mu_0}D.\tag{13}$$

Based on this model the critical thickness is received when the total energies of the two states are identical, i.e., from $\Phi_S=\Phi_\gamma$ and results in $D^{\text{crit}}=0.3$ nm for a square permalloy platelet of edge length 1 μm. In Fig. 11 this analytical result is compared to the corresponding numerical one. Obviously, the analytical calculation overstimates the stray field

energy of the (quasi)homogeneous state. This is not surprising since the C, S, or flowerlike quasi-closure end domains reduce the surface charges. This effect, however, has not been included in the analytical model. In contrast, the wall energy of the four domain state is considerably underestimated by the analytical calculation. The reasons for this are that Eq. (9) is valid for bulk samples and has to be modified for thin platelets, and the vortex itself, which has not been taken into account up to now in the analytical model. Nevertheless, from a qualitative point of view, the analytical model calculation can explain the existence of a critical layer thickness, and also gives the right trends for the appearance of the two phase diagrams illustrated above.

V. CONCLUSIONS

In conlusion, we have set up phase diagrams for a square ferromagnetic thin platelet depending on both thickness and edge length and thickness and magnetic hardness by means of micromagnetic numerical FEM calculations identifying a multidomain phase and a single-domain phase. The critical layer thickness for which the phase transition between the two phases takes place is shifted to significantly larger values when the hardness Q increases, whereas an increasing edge length a of the platelet reduces the critical layer thickness. These results are fundamental for the development of thin film elements in the magnetic recording industry.

[1] S. Tsunashima, J. Phys. D **34**, R87 (2001).

[2] S. S. P. Parkin, K. P. Roche, M. G. Samant, P. M. Rice, R. B. Beyers, R. E. Scheuerlein, E. J. O'Sullivan, S. L. Brown, SL J. Bucchigano, D. W. Abraham, Y. Lu, M. Rooks, P. L. Trouilloud, R. A. Wanner, and W. J. Gallagher, J. Appl. Phys. **85**, 5828 (1999).

[3] S. Tehrani, J. M. Slaughter, E. Chen, M. Durlam, J. Shi, and M. DeHerrera, IEEE Trans. Magn. **35**, 2814 (1999).

[4] G. A. Prinz, J. Magn. Magn. Mater. **200**, 57 (1999).

[5] A. Hubert and R. Schäfer, *Magnetic Domains–The Analysis of Magnetic Microstructures* (Springer-Verlag, Berlin, 1998).

[6] R. Hertel and H. Kronmüller, J. Appl. Phys. **85**, 6190 (1999).

[7] H. Kronmüller and R. Hertel, in *Magnetic Storage Systems Beyond 2000*, edited by G. C. Hadjipanayis (Kluwer, Dordrecht, 2000), p. 345.

[8] W. Rave and A. Hubert, IEEE Trans. Magn. **36**, 3886 (2000).

[9] W. F. Brown, Jr., J. Appl. Phys. **39**, 993 (1968).

[10] A. Aharoni, J. Appl. Phys. **51**, 5906 (1980).

[11] A. Aharoni, J. Appl. Phys. **63**, 5879 (1988).

[12] W. C. Elmore, Phys. Rev. **54**, 1092 (1938).

[13] R. P. Cowburn, D. K. Koltsov, A. O. Adeyeye, M. E. Welland, and D. M. Tricker, Phys. Rev. Lett. **83**, 1042 (1999).

[14] R. P. Cowburn, J. Phys. D **33**, R1 (2000).

[15] W. Rave, K. Fabian, and A. Hubert, J. Magn. Magn. Mater. **190**, 332 (1998).

[16] R. Hertel and H. Kronmüller, J. Magn. Magn. Mater. **238**, 185 (2002).

[17] R. D. McMichael, Standard Problems Number 1–4, Problem Specification and Reported Solutions, Micromagnetic Modeling Activity Group, http://www.ctcms.nist.gov/ rdm/mumag.html, 1998

[18] M. E. Schabes and H. N. Bertram, J. Appl. Phys. **64**, 1347 (1988).

[19] D. R. Fredkin and T. R. Köhler, IEEE Trans. Magn. **26**, 415 (1990).

[20] H. Kronmüller, R. Fischer, R. Hertel, and T. Leineweber, J. Magn. Magn. Mater. **175**, 177 (1997).

[21] R. Fischer, T. Leineweber, and H. Kronmüller, Phys. Rev. B **57**, 10 723 (1998).

[22] T. Schrefl, J. Magn. Magn. Mater. **207**, 45 (1999); **207**, 66 (1999).

[23] R. Hertel and H. Kronmüller, Phys. Rev. B **60**, 7366 (1999).

[24] T. Schrefl, J. Fidler, and H. Kronmüller, Phys. Rev. B **49**, 6100 (1994).

[25] R. Fischer and H. Kronmüller, Phys. Rev. B **54**, 7284 (1996).

[26] V. Novosad, M. Grimsditch, K. Y. Guslienko, P. Vavassori, Y. Otani, and S. D. Bader, Phys. Rev. B **66**, 052407 (2002).

[27] K. Y. Guslienko, V. Novosad, Y. Otani, H. Shima, and K. Fukamichi, Phys. Rev. B **65**, 024414 (2002).

[28] R. Hertel and H. Kronmüller, IEEE Trans. Magn. **34**, 3922 (1998).

[29] NAG-FORTRAN library programs, Numerical Algorithms Group, Ltd., Oxford, 1990.

[30] H. Kronmüller, Z. Phys. **168**, 478 (1962).

[31] W. F. Brown, Jr., J. Phys. Soc. Jpn. **17**, 540 (1962).

[32] A. Aharoni, IEEE Trans. Magn. **27**, 4793 (1991).

[33] X. Brunotte, G. Meunier, and J. F. Imhoff, IEEE Trans. Magn. **28**, 1663 (1992).

[34] A. Aharoni, J. Appl. Phys. **83**, 3432 (1998).

[35] A. Raizer, S. R. H. Hoole, G. Meunier, and J. L. Coulomb, J. Appl. Phys. **30**, 5803 (1990).

[36] D. Lewis and E. Della Torre, IEEE Trans. Magn. **33**, 4161 (1997).

[37] T. Baker, Finite Elem. Anal. Design **25**, 243 (1997).

[38] A. Aharoni, *Introduction to the Theory of Ferrmagnetism* (Oxford Science Publications, Clarendon Press, Oxford, 1996).